

Chapter 3

2D Systems

Two-dimensional cell structures are the simplest cell structures whose topology is non-trivial. They are also the lowest-dimensional cell structures for which a natural notion of curvature can be defined. This chapter focuses on two-dimensional cell structures that evolve via curvature flow. We begin by explaining the materials science background that motivates work on these problems. We then explore some problems and questions that arise in characterizing two-dimensional cell structures and suggest a number of ways of approaching them. Next we describe in detail what it means for a cell structure to evolve through curvature flow, and consider some consequences of this. Last, we describe a method for simulating these systems, analyze the error involved, and report results of our simulations.

3.1 Motivation

The microstructure of most common metals and many ceramics is cellular in nature, as described briefly and illustrated in Chapter 1. It has long been recognized [17, 18] that curvature plays a crucial role in the evolution of these structures, because grain¹ boundaries tend to migrate toward their centers of curvature to reduce their interfacial energy [19]. It was shown that this boundary migration occurs only when grain faces are curved or when grains meet at non-equilibrium angles [20]. When a boundary between two grains is curved, thermal motion causes individual atoms to preferentially migrate away from the convexly shaped grain towards its neighbor, which in effect shifts the position

¹In the materials science literature, individual cells are often called *grains*, their boundaries *grain boundaries* and so forth. In this and the following chapters, we use the terms cell and grain interchangeably.

*The content of this chapter has been adapted from [16].

of the boundary itself away from the convexly-shaped grain. When grain boundaries are flat, thermal motion continues but there is no net migration over time, except than that expected from a random walk. Likewise, when grain boundaries meet at angles other than 120° in the isotropic case, grains with acute angles quickly lose atoms at their sharp tips, which causes angles to change so that they approach an equilibrium in which these angles are 120° . Smith later showed [21] that not only are flat grain boundaries stable, but so are any surfaces whose *mean curvature* is zero. Smith also showed that in the more general case, the particular orientations of the grains will impact the surface tension of the grain boundaries, and consequently the equilibrium angles diverge from 120° in this anisotropic case [22]. Figure 3.1 shows a cell structure in which each grain has an identical pattern, though each grain is oriented differently. Circles represent individual atoms sitting on the triangular lattice. This models real polycrystalline materials, in which all grains have identical crystalline structure, though each grain is oriented differently.

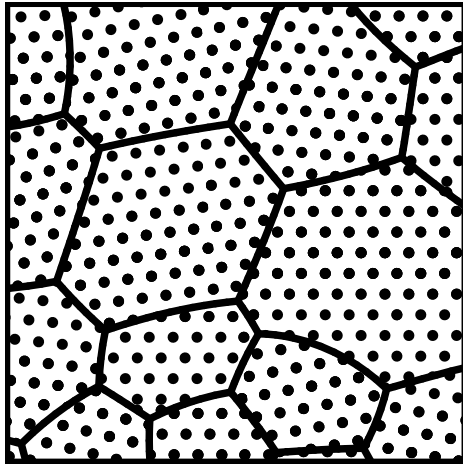


Figure 3.1: Many grains with identical triangular patterns, each with a different orientation. Circles here represent atoms in the individual crystals.

It has also been observed for a long time that polycrystalline materials which evolve through curvature flow exhibit statistical self-similarity. For example, polycrystalline materials have a definite distribution of grain shapes and, after normalization, grain sizes. It is understood that curvature flow shapes cell structures in a way that provides order amongst the otherwise disordered arrangement of grains in the material. Because many of a material’s properties depend strongly on the material’s microstructure — for example its strength and electrical conductivity — a complete understanding of this statistically “universal” structure is very much desired. This requires understanding how cell structures evolve under curvature flow.

The bulk of our work focuses on the problem of *isotropic* grain growth, the simplified case

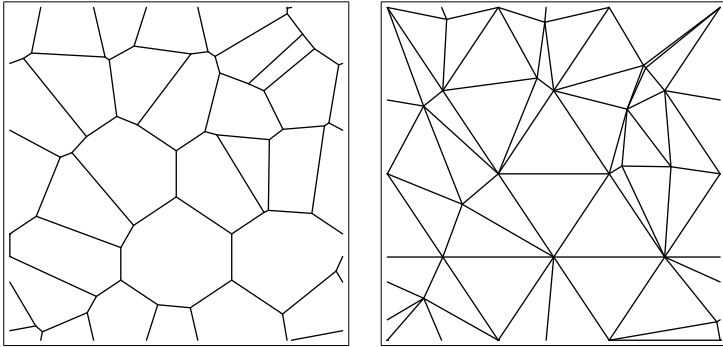


Figure 3.2: A Voronoi tessellation of the unit square torus and its dual Delaunay triangulation.

where the grain boundary energy γ and mobility M are uniform throughout the system. Although almost all materials exhibit some *anisotropy* associated with the oriented nature of individual grains and the relative misorientation between adjacent ones, the isotropic case is still worth considering. From a purely mathematical perspective, this problem raises many interesting questions. Moreover, understanding the isotropic case might provide insight into the more general anisotropic case. Last, the anisotropy of many systems is relatively mild, and so solutions to the isotropic case are reasonable approximations of the real solution.

3.2 Characterization

Here we describe some problems involved in characterizing two-dimensional cell structures. In most physical systems, the number of cells at the system's boundary are far outnumbered by those in its interior. We therefore would like consider a space without boundary. For computational purposes we do not use \mathbb{R}^2 , and because we would like to use an intrinsically flat space we do not consider the standard two-sphere \mathbb{S}^2 . The flat two-torus \mathbb{T}^2 turns out to be the best space to use and in practice we model that using $[0, 1]^2$ with periodic boundary conditions.

Completely characterizing two-dimensional cell structures involves characterizing both their topological² and geometrical features. Much work in describing two-dimensional cell structures has traditionally focused on triangulations, which are roughly dual to the simple cell structures that we consider. Figure 3.2 shows a Voronoi cell decomposition of a flat torus and its dual Delaunay triangulation. Although the number of triangulations of \mathbb{T}^2 are finite for a fixed number of vertices, this number grows exponentially with the number of triangles or cells in the structure. If we only count

²By topological features, we mean those of the cell structure, and not of the underlying space, \mathbb{T}^2 in our case. That is, how the cells are connected and so forth. We sometimes refer to this as the topological characterization, sometimes as the combinatorial characterization. In both cases we mean the same.

cell decompositions with 15 or fewer cells, we already find 1,618,768,888 combinatorially distinct structures! We would like a way of comparing cell structures and describing which ones are more similar or less similar, and not only saying whether or not two are isomorphic.

Before continuing, we point out that the cell structures we consider in this chapter are slightly more limited and slightly more general than those considered elsewhere. First, we only deal with *simple* cell structures. This condition limits the way in which edges can meet: at most three cells can meet at any one point. This would exclude, for example, a map of the United States as divided into states, which includes the four-way meeting between Utah, Arizona, Colorado, and New Mexico. We will explain the motivation for this restriction in Section 3.3. In this sense, the cell structures we



Figure 3.3: Map of the United States with a disallowed, non-*simple* vertex highlighted.

consider are more narrowly defined than those considered elsewhere. We note that triangulations *do* impose this restriction.

On the other hand, the cell structures we consider here are slightly more general than those considered elsewhere. We explicitly allow cells with only two sides, also known as *digons*. Figure 3.4 shows a simple cell structure with a digon in the middle. Although digons do not violate the *simple* condition, they are often avoided for a number of other reasons. A graph containing a digon (or the tessellation of a digon) cannot be 3-connected and therefore, via Steinitz's theorem [23], cannot be the graph of a convex polyhedron. Moreover, the presence of digons introduces irregularities in boundaries of adjacent cells. Without digons, two distinct cells either intersect along an edge or not at all. After digons are introduced, we must generalize this statement: two distinct cells either intersect along a series of edges or not at all. In the figure above, the two cells that are adjacent to the digon intersect one another along more than one edge. These are some of the reasons that digons are often disallowed.

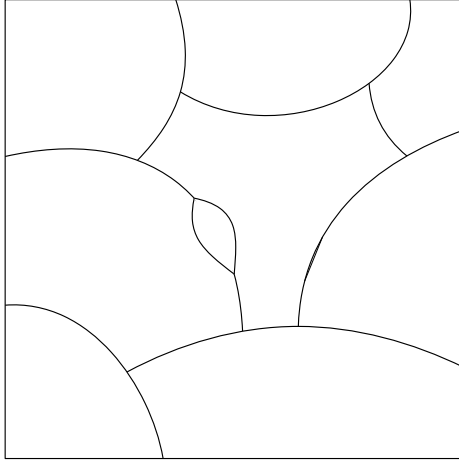


Figure 3.4: A cell structure containing a digon.

With all of these “problems”, why do we allow cell structures containing digons? The reason is because digons actually appear in many physical systems including those we study. Although they complicate our analysis, we must allow them if our systems are to model real physical systems.

One condition we do not impose explicitly yet seems to always be satisfied is this: Every edge is bounded by two vertices. This condition excludes “circular island” cells. We have not found these in any system and we believe that they cannot arise in the physical systems we study.

A few remarks can be made about these systems. According to Euler’s theorem, the number of vertices, edges, and cells are related as follows:

$$\chi = V - E + F, \quad (3.1)$$

where V is the number of vertices, E the number of edges, and F the number of cells; χ is known as the Euler characteristic of the underlying space, and in our case $\chi(\mathbb{T}^2) = 0$. Because every vertex is incident with three edges and every edge is incident with two vertices, we have $2E = 3V$. We can then conclude that $E/F = 3$. Because every edge is adjacent to two cells, the average number of sides per cell is twice that value, i.e. the average number of sides per cell is 6. This places a significant restriction on our cell structures, though still allows for much variety in the distribution of sides per cell.

One way to characterize cell structures is by considering $P(n)$, the probability distribution of cells with $n \geq 2$ number of sides; we can consider this distribution for both finite and infinite systems. We say that a particular probability distribution P is *realizable* if there exists some cell structure with that probability distribution. A natural question to ask is what probability distributions are

realizable? Is any discrete probability distribution whose mean is 6 realizable? We leave for another place answering this question, though point out that a promising lead to answering this question in the affirmative might be found in the work of [24].

Aside from characterizing the combinatorics of a particular cell structure, we also characterize its geometry. That is, even if two cell structures have the same distributions of cell shapes, their geometries can be quite different. In this chapter and later chapters we consider a number of geometric descriptions of cell structures, including the distribution of cell areas and roundness measures. We have noted before that formulating criteria by which we could say that two cell structures are similar or different would be an important accomplishment.

3.3 Curvature flow on 2D cell structures

Curvature flow on curves

In contrast to the last chapter, now we consider only one dynamic that acts on cell structures — curvature flow. Before explaining how curvature flow affects cell structures, we begin by introducing curvature flow on manifolds, the more traditional setting for geometrical flows.

Much interest has arisen over the last thirty years in various types of geometrical flows. The general idea is to consider a differentiable manifold whose metric structure evolves over time via a set of partial differential equations. Inverse mean curvature flow is one particular example that has proven successful in shedding light on general relativity [25] and black holes [26]. A possibly more prominent example is the Ricci flow, which “smooths out” the metric of a Riemannian manifold in a very particular and controlled manner. When considered properly, this study of geometry can help us learn much about the topology of an object. Grigori Perelman recently used this tool to help solve the longstanding Poincaré conjecture regarding the classification of 3-manifolds [27, 28, 29].

In this thesis, we focus on *curvature flow* of planar curves and two-dimensional cell structures, and *mean curvature flow* of embedded surfaces and three-dimensional cell structures. Both of these areas have proven fruitful areas of research in the last thirty years, and we provide a rough sketch of the general ideas and of a few basic, but very beautiful, results in the field. We focus now on curvature flow of planar curves and two-dimensional cell structures, and leave mean curvature flow of surfaces and three-dimensional cell structures for further discussion in the next chapter.

A curve in the plane can be defined as a continuous mapping: $\alpha : I = [a, b] \rightarrow \mathbb{R}^2$. We say that the curve is *closed* if $\alpha(a) = \alpha(b)$. We say that a curve is *simple* if for all $t, u \in (a, b)$, $\alpha(t) \neq \alpha(u)$.

This condition prohibits a curve from crossing itself. Last, a curve is *regular* if $\alpha'(t) \neq 0$ for all $t \in I$.

The arc-length s of a curve α mapped from the interval $[a, b]$ is defined: $s(\alpha) = \int_a^b |\alpha'(t)|dt$. Since the arc-length of a curve does not depend on its parameterization, we choose a parameterization in a way so that the arc-length s of a curve α mapped from the interval $[a, b]$ is always exactly $b - a$. This is called the *arc-length parameterization* of α .

If an arc-length parameterized curve α is simple, closed, and at least twice-differentiable, then $|\alpha'| = 1$ and we can define a notion of curvature as follows. We use $\mathbf{T}(s) = \alpha'(s)$ to denote the unit vector tangent to α at a point $\alpha(s)$ and pointing in the direction in which we traverse the curve. We use $\mathbf{N}(s)$ to refer to the unit vector normal pointing outward from α . We define the unsigned curvature $\kappa(s) = \|\mathbf{T}'(s)\| = \|\alpha''(s)\|$. In the plane we can also give the curvature a sign, depending on which direction the tangent direction is turning. If we are traversing the curve in a counterclockwise fashion, then if the unit tangent vector is turning clockwise then the curvature is negative; if it is turning counter clockwise then the curvature is positive. We use $k(s)$ to denote this signed curvature at a point $\alpha(s)$.

In Figure 3.5 we draw a picture of a curve with a number of $k\mathbf{N}$ vectors drawn at various points along the curve. It can be seen that when the unit tangent changes more sharply, the vectors are

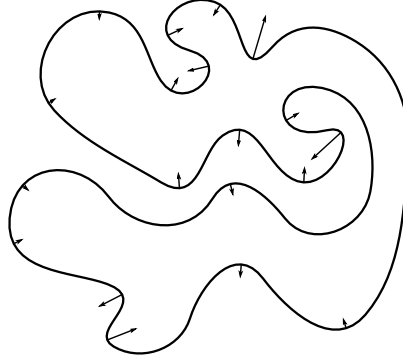


Figure 3.5: A curve with some curvature arrows drawn.

longer (owing to a large κ), and when the unit tangent changes less sharply, the vectors are shorter.

Curvature flow uses this curvature vector $k\mathbf{N}$ to define an equation governing the evolution of the curve. We let $\alpha(\cdot, 0) : S^1 \rightarrow \mathbb{R}^2$ be an embedded, closed planar curve that is at least twice differentiable. We define $\alpha : S^1 \times [0, T) \rightarrow \mathbb{R}^2$ and require that it satisfy the differential equation:

$$\frac{\partial \alpha}{\partial t} = C k \mathbf{N} \quad (3.2)$$

As the parameter t moves through $[0, T)$, the curve “evolves through time”. The variable C allows

the introduction of a constant that might depend on physical properties of the system. Generally speaking we consider isotropic systems in which this variable is uniform throughout a system and over time. Figure 3.6 shows an embedded curve at different points in its evolution. We note two features

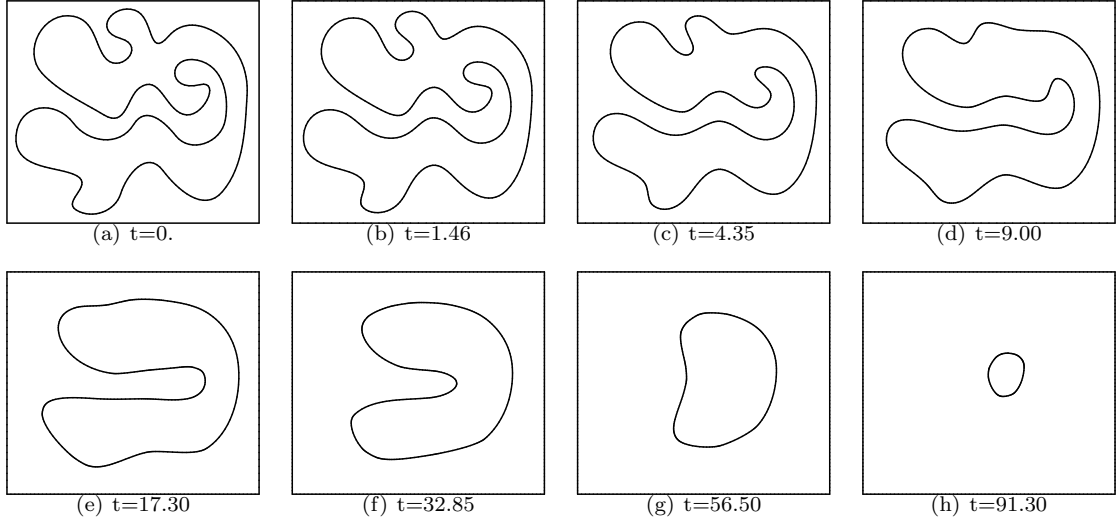


Figure 3.6: A smooth curve embedded in the plane evolves via curvature flow. The area bounded by the curve decreases at a constant rate, and the curve becomes progressively more circular; the curve eventually disappears in finite time.

of this evolution, the first is observable from the illustrations, the second not. One curious feature about this curve is that it seems to evolve toward a circle as it shrinks. A beautiful result of Hamilton, Gage, and Grayson [11, 9] states that *every* embedded curve that evolves through curvature flow becomes convex and asymptotically closer to a circle as it disappears, without developing singularities before disappearing.

A second key feature of the evolution is that way in which its area changes — the area decreases with time at a constant rate independent of the shape of the curve or the area of the bounded region. We adapt a proof of this theorem from the paper of Mullins [30].

Consider a simple smooth curve evolving via curvature flow as described above. We can consider the curve given by polar coordinates, $r(\theta, t)$, where r and θ are the polar coordinates and t is time. To define the signed curvature we choose to traverse the curve counterclockwise and regard the tangent vector as directed in this sense. We use s to refer to the arc length along the curve and β the angle measured in a counterclockwise manner between the positive x -axis and the directed tangent; we use ψ to measure the angle measured in a counterclockwise manner between the polar radius vector and the directed tangent. Any point on the curve moves toward its center of curvature in a manner described by curvature flow, Equation 3.2. We set C in that equation to $M\gamma k$, where

M is the mobility of the grain boundary, γ is its surface tension, and k is the signed curvature at that point. Figure 3.7 shows a solid curve at time t and another dashed curve at a time $t + \Delta t$. It

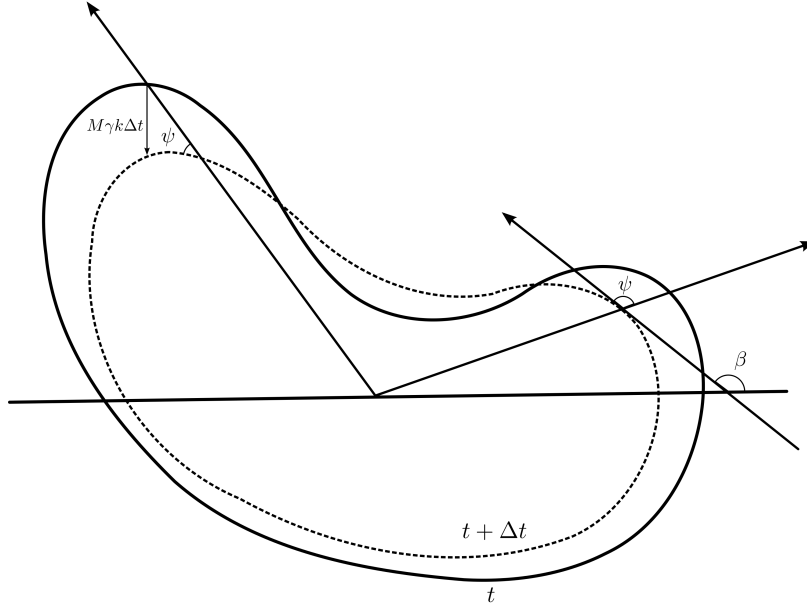


Figure 3.7: A simple closed curve adapted from [30]. The solid closed curve shows $r(\cdot, t)$; the shorter, dashed curve shows $r(\cdot, t + \Delta t)$.

can be seen from the top left part of the illustration that $\Delta r \sin \psi = -M\gamma k \Delta t$. From differential geometry we know that $k = \partial \beta / \partial s$ and that $\sin \psi = r(\partial \theta / \partial s)$. We can then calculate:

$$\frac{\partial r}{\partial t} = -M\gamma \frac{k}{\sin \psi} = -M\gamma \frac{1}{r} \frac{\partial \beta}{\partial \theta} \quad (3.3)$$

The area enclosed by a simple closed curve is given by $A = \frac{1}{2} \oint r^2 d\theta$ where the integral is taken in a counterclockwise sense around the curve. Together with the previous equation, we can calculate the rate of change of the enclosed area:

$$\frac{dA}{dt} = \oint \frac{\partial r}{\partial t} r d\theta = -M\gamma \oint \frac{\partial \beta}{\partial \theta} d\theta = -M\gamma \oint d\beta = -2\pi M\gamma \quad (3.4)$$

The area inside a closed curve thus changes by a constant rate determined only by M and γ . This is the theory of curvature flow on simple closed planar curves. This result will be vital when studying the evolution of cell structures that evolve via curvature flow.

In the next section we describe how curvature flow affects cell structures and derive the von Neumann-Mullins relation which states that the rate of change of cell areas is proportional to six less than its number of sides.

Curvature flow on cell structures

Before deriving the general von Neumann-Mullins relation for cell structures evolving via curvature, we point out and explain two particular features of curvature flow cell structures. Figure 3.8 shows a typical cell structure which has evolved through curvature flow. The first feature worth noting is the

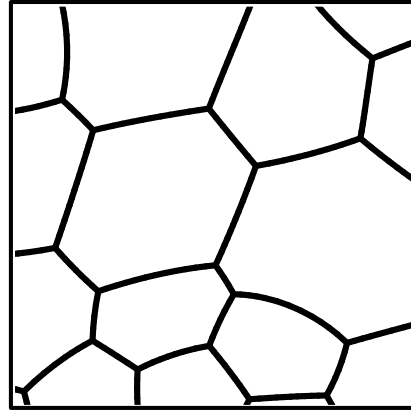


Figure 3.8: A small cell structure.

way in which edges meet: there is no point at which more than three edges meet because such points are “unstable” under curvature flow. Curvature flow is the gradient flow of the length functional and thus minimizes the total length of a curve, which can be seen from the frames in Figure 3.6. In cell systems, curvature flow minimizes the sum of all edge lengths in the structure. For this reason, we almost never find four or more edges meeting at a single vertex, since the total length of this configuration can almost always be reduced by splitting the vertex into two and introducing a new edge between them. Figure 3.9 shows a vertex where four edges meet, and a picture after the vertex

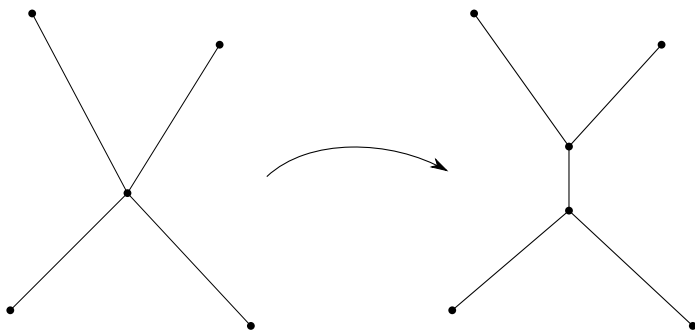


Figure 3.9: Splitting a vertex where four or more edges meet can almost always decrease the total length of the edges.

has been “split” into two. The total length of the edges is smaller after the vertex has been split

and a new edge created. Vertices are thus unstable under this edge length-minimizing flow.

Another feature of interest is the way in which three edges meet at a vertex — the angle between any two edges is always 120° ! The explanation for this phenomenon goes back to an old problem from the 17th century. In a letter to his student, Fermat asked the following question. Consider three points in the plane such that the edges between them do not form any angle larger than 120° .

Figure 3.10 shows such a picture. Now consider adding a fourth point and measure the sum of the

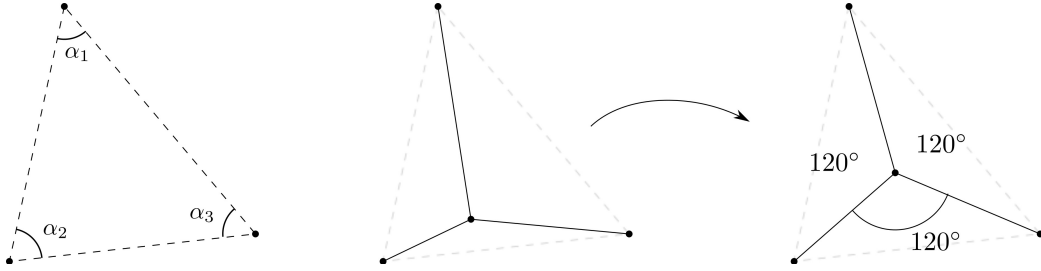


Figure 3.10: A set of three points in the plane such that the edges between them do not form any angle α_i greater than 120° . The sum of edge lengths of all segments from the three points to a fourth point inside the triangle is minimized when the angles between the three segments are all 120° .

distances between the new point and the three initial points. Fermat asked his student Torricelli to find the point which minimizes this sum. It turns out that there is one point that minimizes this sum, and at this point all angles between the edge segments will be 120° ! Since curvature flow minimizes the sum of the edge lengths, vertices will always move in a way that brings them closer to equilibria positions, where the angles are 120° . We note that although grain boundaries move at a finite rate, in an infinitesimal neighborhood of a point, the edges can move infinitely fast, and so the edges can always meet at 120° , even while the structure is evolving at a finite rate.

We can now generalize Equation 3.4 to cases of cells in cell structures, giving us the von Neumann-Mullins relation [31, 30]. Equation 3.4 states that the rate of change of the area enclosed by a simple smooth curve is proportional to the integral of the signed curvature around the curve. Positively signed curvature contributes to the cell's shrinking while negatively signed curvature contributes to the cell's growth. When integrated around the entire curve, the integral of the signed curvature is always 2π . In cells that are part of cell structures and that include non-differentiable "corners", this integral must be reconsidered. Figure 3.11 show a typical example of a cell in a cell structure that evolves via curvature flow. Although the shape is somewhat irregular, internal angles between adjacent edges are always 120° . Therefore, the discrete angle at which the tangent changes at this point is $\pi/3$, as illustrated. Since the points at which three edges meet are in local equilibrium, they do not move and therefore do not contribute to the change in area of the cell. We must then

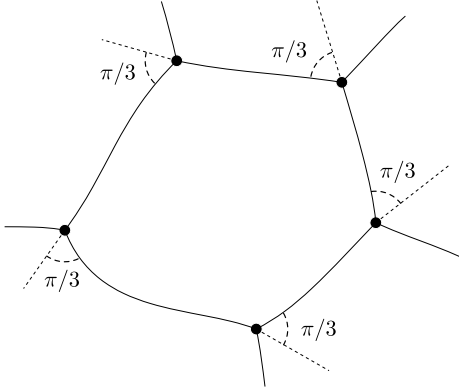


Figure 3.11: A cell with five sides; each pair of cell edges meets at a vertex with an internal angle of 120° .

calculate how much curvature is left around the edges. The signed curvature along the edges and the discrete turning angles must sum to 2π . If each of the n discrete turns is $\pi/3$, then the curvature along the edges themselves is $2\pi - n\frac{\pi}{3}$. Our new equation of motion is then $dA/dt = -M\gamma(2\pi - n\frac{\pi}{3})$, or rewritten in terms of $n - 6$.

$$\frac{dA}{dt} = \frac{\pi}{3} M\gamma(6 - n). \quad (3.5)$$

This form allows us to readily see that grains with more than six sides will grow, those with fewer than six sides will shrink, and those with exactly six sides will neither grow nor shrink (although their shapes may change). This equation is known as the von Neumann-Mullins relation [31, 30] and has deeply influenced understanding of grain growth.

In the next section, we describe a front-tracking method for modeling cell structures that evolve via curvature flow and analyze the error associated with this method. We show that this error is remarkably small, even for a rather coarse discretization of the structure mesh.

3.4 Simulation method

Previous models

Over the last quarter century, numerous methods have been developed to study grain growth in two and three dimensions, including Monte Carlo Potts models [32, 33], cellular automata [34, 35], phase field models [36, 37], vertex models [38, 39], front tracking models [40], finite element models [41], molecular dynamics [42, 43, 15] and level set methods [44, 45, 46, 47]. Each approach has advantages and disadvantages. The Monte Carlo Potts model is both simple, easily implementable and extendable to a wide range of grain growth phenomena. Phase field models, like the Potts model, are

based upon well-founded microscopic physics but have the advantage of being formulated in terms of continuum descriptions. Vertex models have the most compact data sets and, arguably, are based on the most fundamental objects in the microstructure — triple-junctions. Front tracking models have the advantage of well-defined equations of motion for boundary elements. Finite element methods naturally carry all material point information. Molecular dynamic simulations require an accurate understanding of the forces between atoms in the material and require enormous resources of memory and time to simulate macro-scale phenomena. In all cases, a discretization of the microstructure is involved, which necessarily compromises our ability to model the requisite grain growth physics in full fidelity.

A widely used numerical scheme for studying the evolution of surfaces, including those of cell structures, is the front tracking method as realized in the robust and versatile program Surface Evolver, developed by Brakke [48]. This program can track the evolution of grain boundaries moving via curvature flow in any number of dimensions. Several papers report grain growth simulation results based upon this method [49, 50, 51]. In this section, we develop a new approach for simulating grain growth that is based on front tracking ideas and that satisfies the von Neumann-Mullins relation at all times with very small error, regardless of discretization. In this chapter, we implement this new grain growth method in two dimensions and compare our results with those obtained using the Surface Evolver program. In Chapter 4 we will extend this method to three dimensions.

Proposed model

In Chapter 2 we considered four different initial conditions from which we began our simulations. This allowed us to demonstrate the existence not only of steady states but also of universal steady states, i.e. states to which almost all initial systems evolved after they had evolved for sufficient time. The increase in dimension significantly limits our simulations and in this chapter and the next we focus on data collected from simulations that begin with only one particular initial condition.

In two dimensions, we begin all simulations from a Voronoi tessellation. This construction involves placing “seeds” in the unit square and associating with each seed a particular region of the space. In practice, we choose N pairs of random variables from a uniform probability distribution on the interval $[0, 1)$. These two random numbers become the x and y coordinates for a seed. With each seed we associate all points in the unit square that are closer to that seed than to any other seed. All points associated with one seed constitute a single cell. The simplicity of this construction allows its use in arbitrary dimension, and indeed we use this construction in the next chapter, in studying

three-dimensional systems, as well. Figure 3.12 illustrates the construction of such a system with 1000 cells.

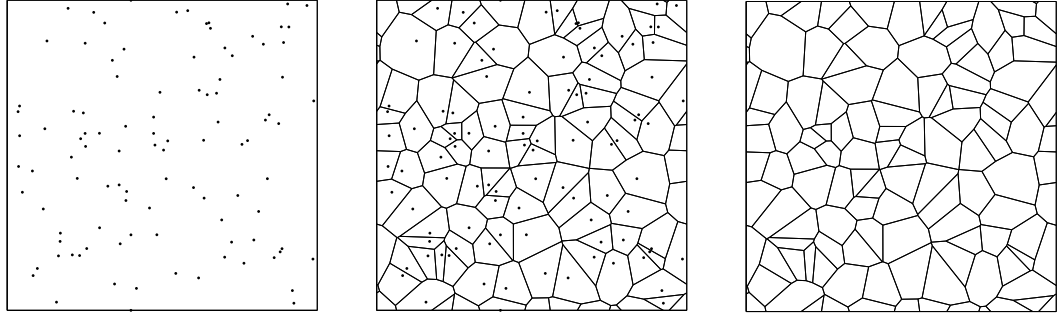


Figure 3.12: Constructing a Voronoi tessellation of $[0, 1]^2$ with periodic boundary conditions. Here we choose 100 points independently and randomly distributed, from a uniform probability density distribution on $[0, 1]^2$; these points are *seeds*. To each seed we associate all points in the space that are closer to that seed than to any other seed. All points associated with one seed constitute a single cell. We draw lines to show the boundaries between cells. We then discard the original seeds.

Data representation

Every grain is represented as an ordered list of points which lie along the boundary of the grain. Points located where three grains meet are called *triple-nodes*; points located along grain boundaries but that are adjacent to only two grains are called *boundary nodes*. Straight line segments connect adjacent boundary nodes and are called *edge segments*. Figure 3.13 shows two 5-sided grains surrounded by a few other grains. Larger dots and smaller dots are used to indicate triple-nodes and boundary nodes, respectively. Boundary nodes are occasionally added to make the discretization

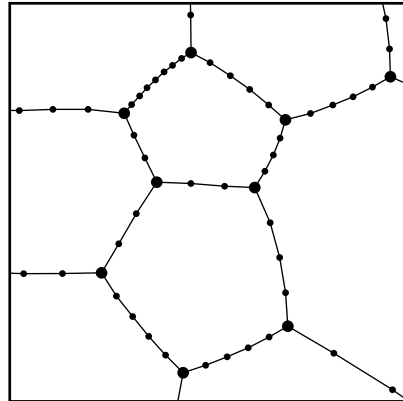


Figure 3.13: Two 5-sided grains with a few neighboring cells. Each edge is broken into a few edge segments. Larger dots indicate the triple-nodes; smaller dots indicate the boundary nodes.

smoother, or removed when neighboring ones become too close. Each node in the system is represented by a data object which stores the node's x and y coordinates, its velocity, and some data about its neighboring grains and nodes. Each grain is represented by a data object which stores an ordered list of the nodes which make up the grain's boundary, as well as data about the grain's area, perimeter, and information about its neighboring grains.

Node motions

We develop a method for moving nodes in a manner that ensures that the von Neumann-Mullins relation is satisfied for all grains at all times with minimal error. To do this, we discretize the time variable t from Equation 3.5 into time steps Δt and solve for the change in grain area ΔA :

$$\Delta A = \frac{\pi}{3} M\gamma (6 - n) \Delta t. \quad (3.6)$$

For simplicity, we consider a discretization of a single isolated grain, illustrated in Figure 3.14. All nodes here should be considered boundary nodes. Moving the node σ changes the area of the shaded

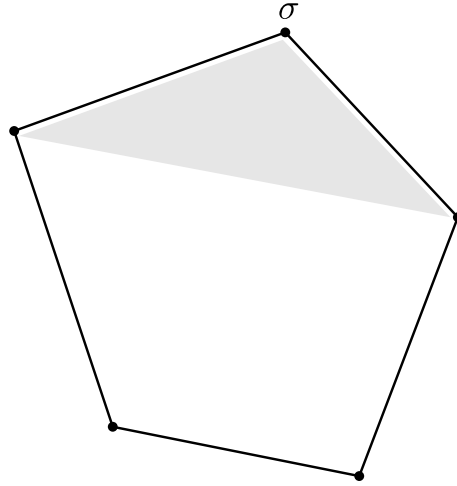


Figure 3.14: An isolated grain with no triple-nodes.

triangle by the same amount as it changes the area of the entire grain. This ability to localize changes of area enables us to express each side of Equation 3.6 as a sum over all nodes surrounding a grain. The sum of the exterior angles around a discretized grain (a polygon) is exactly 2π . If we ensure that the area of each triangle changes by an amount $-\alpha M\gamma \Delta t$, where α is the exterior angle at its apex, then after each time step the area of the entire polygon will change by $-2\pi M\gamma \Delta t$, with an error of order $(\Delta t)^2$, owing to overlap between triangles associated with adjacent nodes; this error will be elaborated in detail in the next section. We point out that if moving a boundary node changes the

area of one adjacent grain by ΔA , then it also changes the area of the other adjacent grain by $-\Delta A$.

We now shift attention to the case of triple-nodes, which we treat as boundary nodes with one correction. That is, we move triple-nodes in a way that changes the area of each neighboring grain by an amount $-(\alpha_i - \frac{\pi}{3})M\gamma\Delta t$. Since a grain with n neighbors has n triple-nodes, the area of a grain with n neighbors will change by an amount $-(2\pi - n\frac{\pi}{3})M\gamma\Delta t$, or $\frac{\pi}{3}M\gamma(n - 6)\Delta t$, which is exactly the discretized von Neumann-Mullins relation for n -sided bodies, Equation 3.6.

We now provide a more precise description of the motion of each node, beginning with boundary nodes. Consider a boundary node σ with edges \mathbf{e}_1 and \mathbf{e}_2 , as shown in Figure 3.15. The exterior angle between the two edges is $\alpha = \cos^{-1}(-\frac{\mathbf{e}_1 \cdot \mathbf{e}_2}{|\mathbf{e}_1||\mathbf{e}_2|})$. Our goal is to move node σ by a displacement

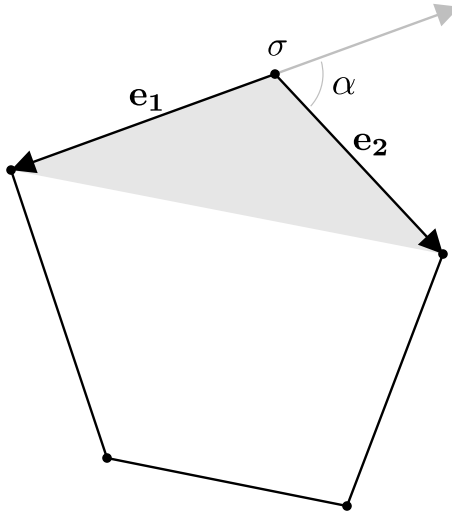


Figure 3.15: A schematic of an isolated grain, emphasizing a boundary node σ and directed edges \mathbf{e}_1 and \mathbf{e}_2 .

vector \mathbf{dv} that will change the area of the shaded triangle by $\Delta A = -\alpha M\gamma\Delta t$. Although we could move the node in many different directions (with an appropriate magnitude) to achieve the desired area change, for reasons of numerical stability we move the node in the direction of $\mathbf{e}_1 + \mathbf{e}_2$. If α is the turning angle, or exterior angle, between the two edges, then to change the area of the triangle by exactly $-\alpha M\gamma\Delta t$, we let:

$$\mathbf{dv} = \alpha M\gamma\Delta t \frac{\mathbf{e}_1 + \mathbf{e}_2}{|\mathbf{e}_1 \times \mathbf{e}_2|}. \quad (3.7)$$

We next consider a triple-node τ where three grains meet, as shown in Figure 3.16. To satisfy the von Neumann-Mullins relation, displacement of the triple-node must change the area of each neighboring grain by $\Delta A_i = -(\alpha_i - \frac{\pi}{3})M\gamma\Delta t$, where α_i is the exterior angle at the triple-node with respect to grain i . Unlike boundary nodes, which have a degree of freedom in their solution, triple-nodes have exactly one solution. If $\alpha_1 = \cos^{-1}(-\frac{\mathbf{e}_1 \cdot \mathbf{e}_2}{|\mathbf{e}_1||\mathbf{e}_2|})$, $\alpha_2 = \cos^{-1}(-\frac{\mathbf{e}_2 \cdot \mathbf{e}_3}{|\mathbf{e}_2||\mathbf{e}_3|})$, and $\alpha_3 =$

$\cos^{-1}(-\frac{\mathbf{e}_3 \cdot \mathbf{e}_1}{|\mathbf{e}_3||\mathbf{e}_1|})$ then solving:

$$\begin{bmatrix} \mathbf{e}_1 - \mathbf{e}_2 \\ \mathbf{e}_2 - \mathbf{e}_3 \\ \mathbf{e}_3 - \mathbf{e}_1 \end{bmatrix} \mathbf{d}\mathbf{v} = 2M\gamma\Delta t \begin{bmatrix} \alpha_1 - \frac{\pi}{3} \\ \alpha_2 - \frac{\pi}{3} \\ \alpha_3 - \frac{\pi}{3} \end{bmatrix} \quad (3.8)$$

for $\mathbf{d}\mathbf{v}$ will tell us exactly how to move the triple-node τ . Although this system may initially appear overdetermined, inspection will show that exactly two equations are independent, and so there will always be exactly one solution for $\mathbf{d}\mathbf{v}$.

Equations 3.7 and 3.8 then describe the motions of all boundary nodes and all triple-nodes, respectively. These equations represent the displacement vectors for each node at every time step. More details regarding the two-dimensional method are provided in Appendix B.

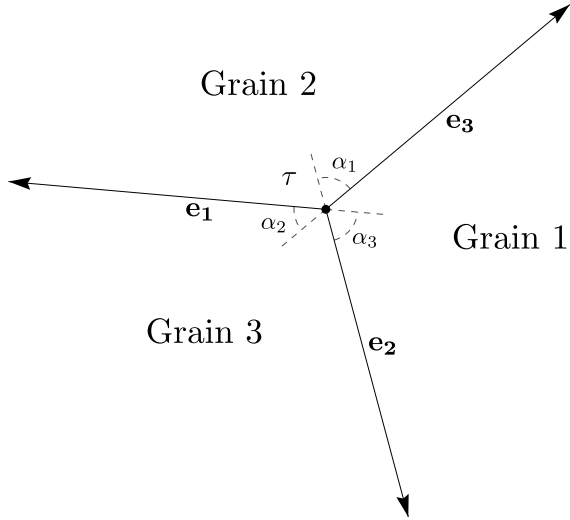


Figure 3.16: A triple-node τ where Grains 1, 2, and 3 meet, where \mathbf{e}_i are the vectors from the triple-node to the nearest nodes on each of the three boundaries, and α_i are the “turning angles”, or exterior angles with respect to each of the three grains.

It is worth explaining here an important difference between our method and other front-tracking methods. At first sight, the motions described above may not resemble motion by curvature flow: we do not attempt to move nodes in their normal directions and with a magnitude proportional to their local curvature. Indeed, a more naive approach may attempt to define a normal direction at every node, and move each node in that direction by an amount proportional to the mean curvature at that point. The problem is that although this method might accurately describe the displacements of a finite set of points in the system, where the nodes are placed, it does not adequately describe

the motion of any other point in the system. In the current method, rather than considering the velocities of a finite set of points and moving the surface as those points require, we consider the way in which the area of a grain changes with the movement of entire sections of the boundary. In this way, our method allows us to satisfy the exact von Neumann-Mullins relation without resorting to an arbitrarily refined surface mesh.

Topological changes

Aside from calculating the velocities of all nodes in the system, we also must change the local “topology” from time to time. Edges and entire grains shrink and disappear, and the network must be adjusted accordingly. In two dimensions, the number of topological changes is fairly limited. The most frequent topological change is the switching of an edge lying between two grains and adjacent to two other grains. Figure 3.17(a) shows the “neighbor-switching”, or T1, process [52]. The second

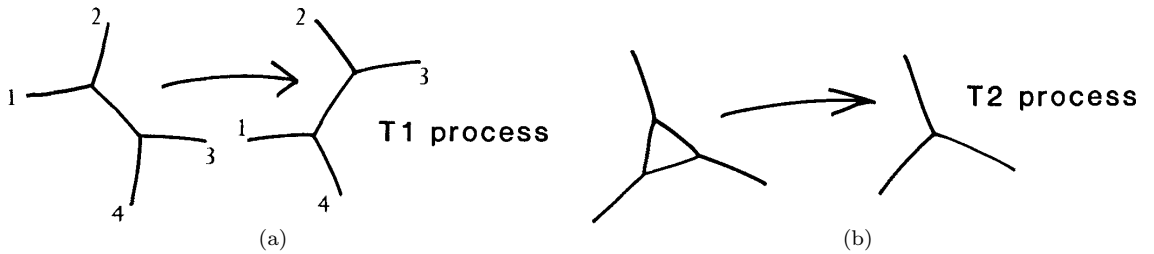


Figure 3.17: Illustrations of T1 and T2 processes; figures taken from [52].

most frequent topological change is the removal of a three-sided grain, illustrated in Figure 3.17(b). In this process, three edges and triple-nodes shrink down to one triple-node.

Weaire and Kermode, the authors who first named the T1 and T2 processes [53, 52] noted that C.S. Smith [54] had asserted many years earlier that all shrinking cells eventually become three-sided and then disappear as such. In other words, Smith believed that a two-sided grains could not arise in a cell-structure evolving through curvature flow if it did not exist in the initial structure. In an appendix to that same paper [53], the authors point out that experimental results of two-dimensional soap foams reported in [55] contain no two-sided grains and they argue based on theoretical grounds why this should generally be the case. Although they report two-sided grains in their own simulations, they attribute this to numerical error.

However, other early papers [56, 57, 58] have noted the presence of two-sided grains and their disappearance in computer simulations, and believe that their occurrence is not due merely to numerical error. We also find such grains in our simulations and believe that such grains can arise

in real systems. The disappearance of a two-sided grain is often called a T3 process [58, 59, 60, 61] and is illustrated in Figure 3.18.

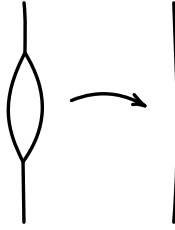


Figure 3.18: T3 process.

Implementing each of these changes in our code is relatively simple. If we observe that a certain edge is shrinking too fast, we decide to implement a T1 change and begin by removing all boundary nodes along that edge. Next, we remove the two triple-nodes associate with the edge that we are deleting, and create two new ones. We attach edges appropriately, as illustrated in Figure 3.17(a). The locations of the two new nodes are such that the new edge is perpendicular to the old edge and its length is roughly the same. Occasionally we run into trouble with the local geometry and adjust the length of the new edge in a way to make it “fit nicely” into the local structure.

Implementing a T2 change is also straightforward. We first remove all boundary nodes along the grain’s boundary. Next we create a new triple-node at the geometric center of the grain’s three corner nodes. We then attach the three nodes which had been the corners of this grain to the new triple-node, and then adjust the data structures of the three adjoining grains appropriately. Last, we remove the data object associated with the grain itself.

Implementing the T3 change is also very straightforward. We begin by removing all boundary nodes along the grain’s boundary. Next we create a new edge between the two corner nodes which had been the corners of the this grain and adjust accordingly the neighboring grains. Last, we remove the data object associated with the two-sided grain.

More complicated topological changes can be decomposed into series of such changes as already noted in [52]. For example, a four-sided grain that is shrinking can be removed by a T1 process, followed by a T2 process. In a similar way it seems that all topological changes to the system can be decomposed into a series of these three changes. In theory, we could decompose a T2 change into a T1 and T3 change. That is, a triangle can be first changed into a two-sided grain using a T1 change and then removed as a two-sided grain with a T3 change. However, it seems that T2 changes indeed occur, and their decomposition seems unnatural. It is not clear whether or not a 4- or 5-sided grain can really disappear as such, or whether the occurrences of these in simulations is only a result of

numerical error. It would be nice to prove what topological events can occur during curvature flow on cell structures in a continuous setting.

3.5 Error analysis

One strength of our method is the low error inherent in the refinement of the time step and the surface mesh. We first deal with the error associated with the time step, which is of order $O(\Delta t^2)$. We also derive the error associated with Brakke's method [48], and find that error to be of order $O(\Delta t)$.

We define the error as follows. After one time-step, the area of an individual grain *should* change exactly:

$$\Delta A = -2\pi M \gamma \left(1 - \frac{n}{6}\right) \Delta t. \quad (3.9)$$

as explained earlier. We define the error to be the difference between this exact, theoretical result and what actually happens to a grain after one time-step. If ΔA_B is the change in area of a grain after one time-step of size Δt using the Brakke method, then the absolute error is $E_B = |\Delta A - \Delta A_B|$; the relative error is $\epsilon_B = |E_B/\Delta A|$. Likewise, if ΔA_P is the change in area of a grain after one time-step using the proposed method, then the absolute and relative errors are $E_P = |\Delta A - \Delta A_P|$ and $\epsilon_P = |E_P/\Delta A|$, respectively.

We first show that the absolute numerical error involved in our method is of order $O(\Delta t^2)$. To do so, we consider moving an individual node to change the area of a grain by $-\alpha M \gamma \Delta t$ in the case of a boundary node or $-(\alpha_i - \frac{\pi}{3}) M \gamma \Delta t$ in the case of a triple-node. If we keep all other nodes fixed, there is no error (up to machine precision). This is because the proposed method moves the nodes in a manner that is consistent with the exact von Neumann-Mullins relation, as explained above.

If we move all nodes simultaneously, errors result from “interference” between motions of neighboring nodes. Consider for example the edge segment shown in Figure 3.19. If we move only node n_1 by \mathbf{dn}_1 and leave all other nodes fixed, the area of the grain will change by exactly $-(a + b + c)$. Similarly, if we move only n_2 by a motion \mathbf{dn}_2 , leaving all other nodes fixed, the area of the grain changes by $-(c + e + f)$. When we move both nodes simultaneously, we want to change the area of the grain by $a + b + 2c + e + f$. However, the simultaneous motions of nodes n_1 and n_2 instead change the area of the grain by $a + b + c + d + e + f$. This produces an absolute error $|d - c| = \frac{1}{2}|\mathbf{dn}_1 \times \mathbf{dn}_2|$. Since each \mathbf{dn}_i is linear in Δt , the cross product $\mathbf{dn}_1 \times \mathbf{dn}_2$, and hence the the error resulting from the “interference” of the two motions, is linear in $(\Delta t)^2$.

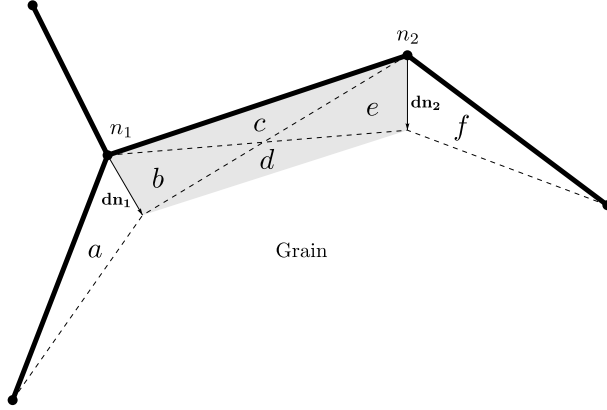


Figure 3.19: Representation of part of an edge between two bodies.

Similar errors occur for all pairs of adjacent nodes moving simultaneously. Because all grain have a finite number of these “interference” errors, the total error involved in the motion of all nodes of one grain will be $O(\Delta t)^2$. More precisely, the error is given by:

$$E_P = \frac{1}{2} \left| \sum_{i=1}^N \mathbf{d}\mathbf{n}_i \times \mathbf{d}\mathbf{n}_{i+1} \right|, \quad (3.10)$$

where the summation is over all node motions $\mathbf{d}\mathbf{n}_i$ of a particular grain.

In the Brakke method, the displacements of the nodes are also linear in Δt , and so it too produces “interference” errors of order $(\Delta t)^2$. However, in the Brakke case, the displacement of each node results in errors that are $O(\Delta t)$ even when all other nodes are fixed. When summed over all nodes in a grain, we have a total error that is also of order $O(\Delta t)$. We demonstrate this for the case of a grain shaped like a regular polygon.

Consider an isolated grain represented by a regular polygon of m sides and radius r , as shown in Figure 3.20. The area of this grain is $\frac{1}{2}mr^2 \sin\left(\frac{2\pi}{m}\right)$. After one time-step, the area of this shape should change by $\Delta A = -2\pi M\gamma\Delta t$, as explained above. In the Brakke scheme³, evolution by one time-step changes the radius r of the grain by $-\frac{M\gamma\Delta t}{r \cos\left(\frac{\pi}{m}\right)}$, while in the proposed method, evolution by one time-step changes the radius by $-\frac{2\pi M\gamma\Delta t}{mr \cos\left(\frac{2\pi}{m}\right)}$. The corresponding changes in the grain area

³We used the `area normalization` and `effective area` options in Surface Evolver. These options are meant to approximate motion by mean curvature. With these options, resistance to motion of a node is proportional to the component of the area associated with that node which is also perpendicular to the force on the node. This method is explained in greater detail in Appendix B and in [62].

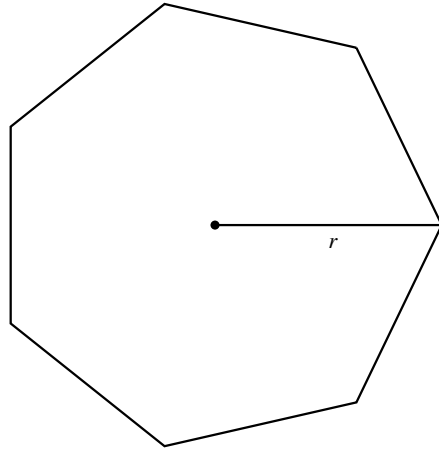


Figure 3.20: Regular polygonal grain with m sides and of radius r .

are

$$\Delta A_B = -M\gamma \left[2m \sin\left(\frac{\pi}{m}\right) \Delta t - \frac{m}{r^2} \tan\left(\frac{\pi}{m}\right) (\Delta t)^2 \right] \quad (3.11)$$

$$\Delta A_P = -M\gamma \left[2\pi \Delta t - \frac{2\pi^2 (\Delta t)^2}{mr^2 \sin\left(\frac{2\pi}{m}\right)} \right]. \quad (3.12)$$

The absolute and relative errors are therefore

$$E_B = M\gamma \left[\left(2\pi - 2m \sin\left(\frac{\pi}{m}\right) \right) \Delta t + \frac{m}{r^2} \tan\left(\frac{\pi}{m}\right) (\Delta t)^2 \right] \quad (3.13)$$

$$E_P = M\gamma \left[\frac{2\pi^2 (\Delta t)^2}{mr^2 \sin\left(\frac{2\pi}{m}\right)} \right] \quad (3.14)$$

$$\epsilon_B = \left(1 - \frac{m}{\pi} \sin\left(\frac{\pi}{m}\right) \right) + \frac{m}{2\pi r^2} \tan\left(\frac{\pi}{m}\right) (\Delta t) \quad (3.15)$$

$$\epsilon_P = \frac{\pi \Delta t}{mr^2 \sin\left(\frac{2\pi}{m}\right)}. \quad (3.16)$$

The absolute error in the Brakke method has a leading order term proportional to Δt for all m ; the relative error has a leading order term entirely independent of the time-step Δt ! On the other hand, in the proposed method, the leading order term in the absolute and relative errors are $(\Delta t)^2$ and Δt , respectively.

To show the difference in scale between ϵ_B and ϵ_P , we evaluate Equations 3.15 and 3.16 for a fixed radius r and time step Δt taken from a typical simulation when 20,000 grains remain. With 20,000 grains, the approximate average radius of a grain is $r = 0.003989L$ and the step size is $\Delta t = 1.21 \times 10^{-9} M\gamma L^2$. Table 3.1 shows relative errors calculated for the two methods with different values of m . Clearly, the relative error in the proposed method is several orders of magnitude smaller

than in the Brakke method.

| m | ϵ_B | ϵ_P |
|-----|--------------|--------------|
| 3 | 17.31% | 0.00919% |
| 4 | 9.97% | 0.00597% |
| 5 | 6.46% | 0.00502% |
| 6 | 4.51% | 0.00459% |
| 7 | 3.33% | 0.00436% |
| 8 | 2.55% | 0.00422% |
| 9 | 2.02% | 0.00413% |
| 10 | 1.64% | 0.00406% |
| 11 | 1.36% | 0.00401% |
| 12 | 1.14% | 0.00398% |

Table 3.1: Relative errors ϵ calculated for the change in area of a grain discretized into m segments using the Brakke method and that proposed here, using Equations 3.15 and 3.16. The errors are calculated for a regular polygon grain with radius $r = 0.003989L$ and a step size $\Delta t = 1.21 \times 10^{-9}M\gamma L^2$.

Similar results can be obtained for grains with different numbers of neighbors. These calculations show that for both vertex and non-vertex nodes, the Brakke scheme produces an absolute error that is, to leading order, proportional to Δt , while in the proposed method the absolute error is proportional to $(\Delta t)^2$. Examination of Equations 3.13 through 3.16 shows that both methods lead to identical errors in the limit where the number of sides m tends to infinity.

3.6 Results

Microstructure Evolution

The evolution of a typical microstructure using the proposed method is shown in Figure 3.21; the microstructure began as a Voronoi tessellation based on 1000 randomly distributed seed points. The initial microstructure has grains with straight edges and triple-nodes where three edges do not generally meet at $2\pi/3$. However, after a short time, the triple-node angles become very close to $2\pi/3$ and many of the boundaries are curved. The structure coarsens over time resulting in fewer grains and a larger average grain size. Figure 3.22 shows a comparison of two microstructures, starting from the same Voronoi initial condition state, where one has been evolved using the method developed by Brakke and the other has been evolved using the method proposed here. While the microstructures appear similar, a grain-by-grain comparison shows that they are microscopically quite different. In the following sections, we offer more quantitative descriptions of these systems that highlight the differences between the two evolution methods.

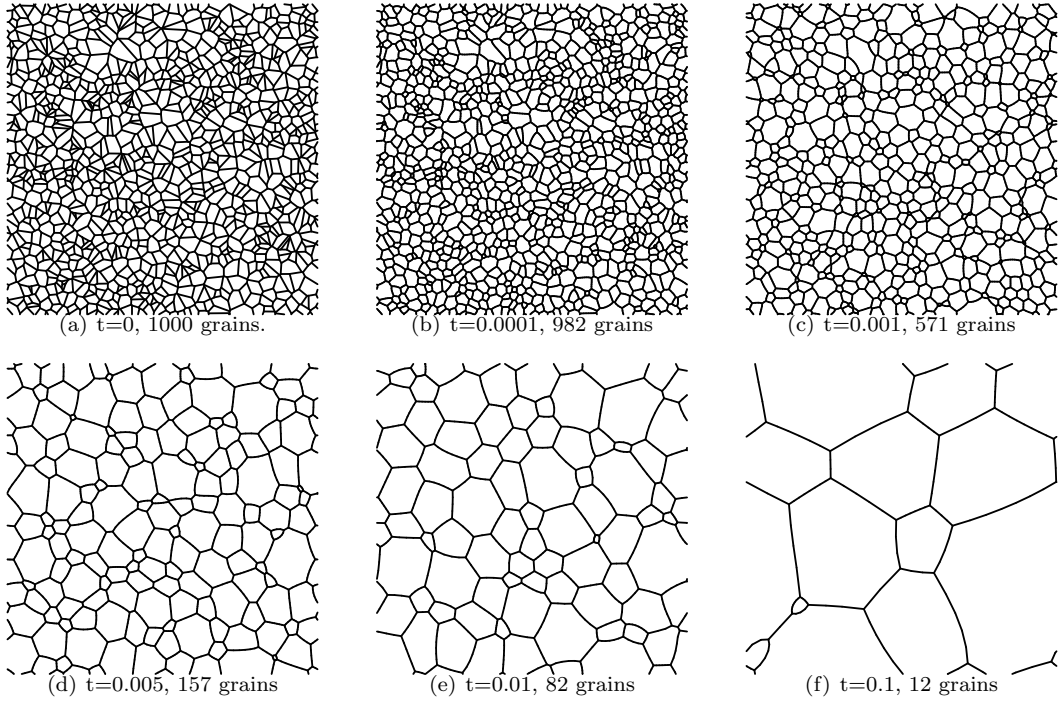


Figure 3.21: Temporal evolution of a microstructure based upon the proposed method for $M\gamma L^2 = 1$. This microstructure was initialized as a Voronoi tessellation of the unit square into 1000 grains.

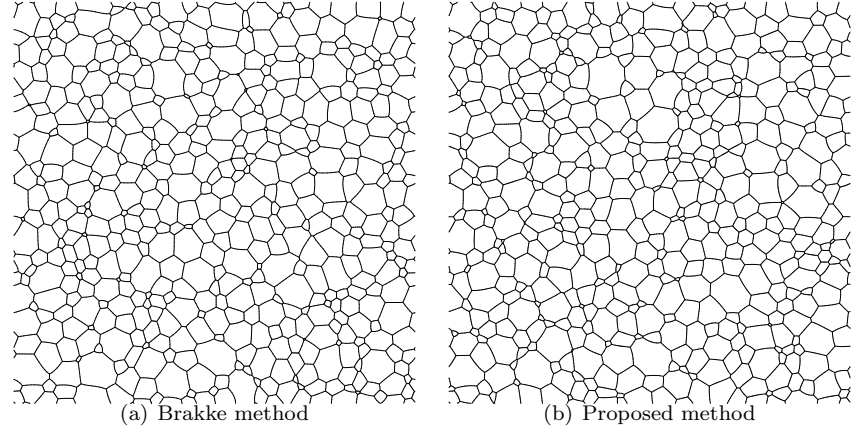


Figure 3.22: Microstructures evolved from a single Voronoi tessellation of 1000 grains after half of the grains have been consumed, using (a) the Brakke method and (b) the proposed method.

Grain Size Evolution

While the microstructure generated using the Brakke method and that generated using the method proposed here appear similar, the comparison presented above is not quantitative. In this section we look at how the average grain size changes over time using these two approaches. To this end, we

simulate the evolution of four different microstructures using the two approaches, each initialized by Voronoi tessellations based on random distributions of 25,000 points. For each method we considered two cases: a refined system, where each grain boundary is represented by approximately 5 line segments (i.e., placing 4 boundary nodes between each pair of triple-nodes) and an unrefined system, where nodes are placed only at points where three grains meet. We evolved these system until 1000 grains remained.

Figure 3.23 shows the change of the average grain area over time, averaged over four runs, for each of the four cases described above: Brakke method-refined, Brakke method-unrefined, proposed method-refined, and proposed method-unrefined. In all four cases, the average grain size appears to

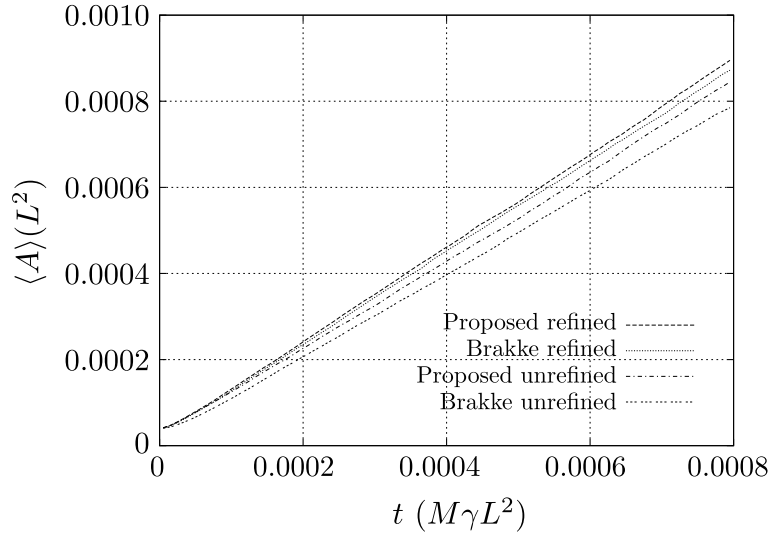


Figure 3.23: The temporal evolution of the average grain area $\langle A \rangle$ for the four cases described above; four samples were run for each case and the averages are plotted. Each system began with 25,000 grains; when $t = 0.0008$, there remain slightly more than 1000 grains. The typical error is about two or three times the size of the dots; the errors are not shown for the sake of clarity.

grow linearly with time, albeit at slightly different rates. For the refined cases shown in Figure 3.23, the slopes of the curves are 1.067 and 1.092 for the Brakke and proposed simulations, respectively. While these slopes are close to 1, we know of no rigorous analytical results that predict them; both are close to the 1.12 ± 0.04 reported in [58]. See also [63] which records slopes ranging from 0.5 to 20 obtained by various other methods and reported elsewhere.

While these results show the evolution behavior of entire systems, the exact von Neumann-Mullins relation (Equation 3.5) describes how each individual grain evolves; i.e., at a constant rate that depends only on its number of sides. Figure 3.24 shows the area growth rates at a single time step for each of the 20,000 grains in a system that was evolved from a 25,000 grain Voronoi microstructure using the Brakke and proposed methods together with a refined discretization. When

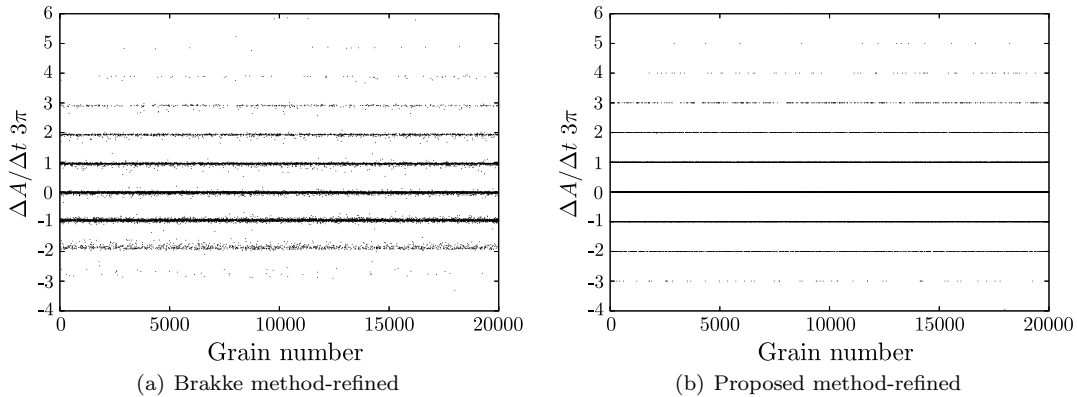


Figure 3.24: Area growth rates $\Delta A_i/\Delta t$ for each grain in a 20,000 grain system for one time step using a refined discretization using (a) the Brakke method and (b) the proposed method. We assign a random number to each grain. In this simulation $M\gamma = 1$.

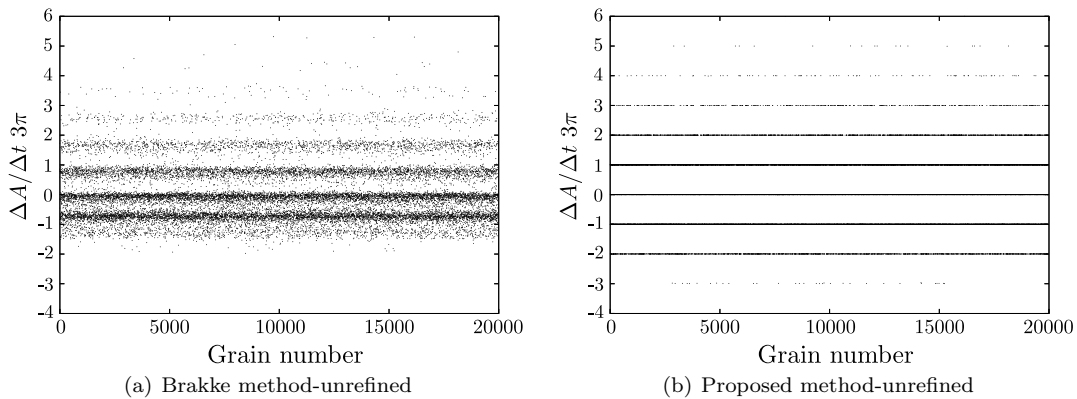


Figure 3.25: Area growth rates $\Delta A_i/\Delta t$ for each grain in a 20,000 grain system for one time step using an unrefined discretization using (a) the Brakke method and (b) the proposed method. We assign a random number to each grain. In this simulation $M\gamma = 1$.

$M\gamma = 1$, these figures should show sharp, horizontal lines at integer values of $\frac{3\Delta A}{\pi\Delta t}$, where each line corresponds to a different number of grain neighbors n . Figure 3.24(b) is an excellent description of the results for the proposed method. However, there is discernible scatter in the data for the Brakke method results, Figure 3.24(a). Furthermore, the average values of $\frac{3\Delta A}{\pi\Delta t}$ differ slightly from the von Neumann-Mullins prediction that these should all be integers.

Figure 3.25 shows results similar to those shown in Figure 3.24, but for the unrefined discretizations which contain boundary nodes. The proposed method shows results that accurately match the von Neumann-Mullins relation even in this unrefined discretization. However, the scatter in the results from the Brakke calculations is very much increased compared with that for the refined discretization. Even more problematic is that the mean position of each set of horizontal lines in

Figure 3.25(a) is in strong disagreement with the prediction of the von Neuman-Mullins exact relation. This again emphasizes the necessity for maintaining a sufficiently refined discretization in the Brakke calculations. The robustness of the proposed method for *any* discretization is one of its main advantages.

The data in Figures 3.25(a) and 3.25(b) can be summarized in a plot of $\Delta A/\Delta t$ versus n . Figure 3.26 shows data collected from a microstructure beginning with 10,000 grains and evolving until 5000 grains remain, using both refined and unrefined discretizations. The best fit line through each set of data is $\frac{3\Delta A}{\pi t} = 0.99997n - 5.9998$. The errors here, provided by comparing this equation with Equation 3.6, are several orders of magnitude smaller than the 1 – 3% errors reported in [58, 64]. That the results are so accurate even for the unrefined microstructure demonstrates another strength of the proposed method.

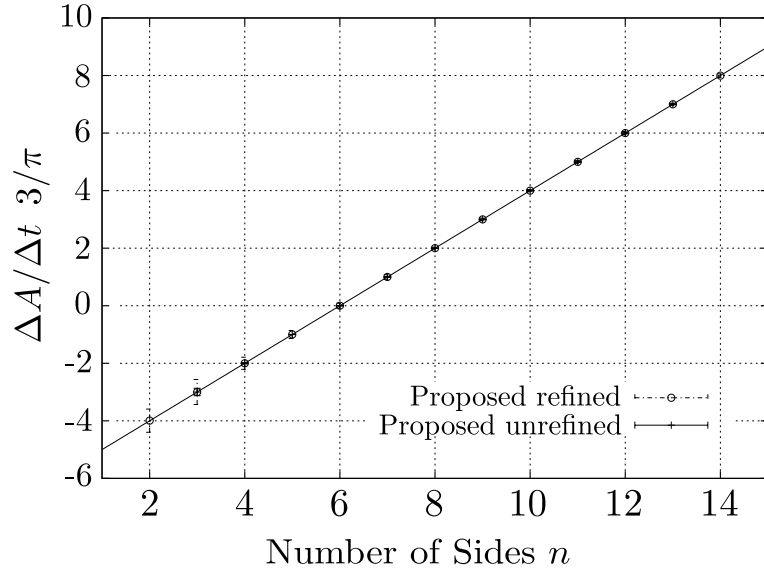


Figure 3.26: Validation of the von Neumann-Mullins relation from data obtained using the proposed simulation method with both a refined and an unrefined discretization; $M\gamma$ is set to 1. The von Neumann-Mullins relation predicts that the points will fall on the line shown. The points here represent data averaged over all grains and time steps in simulations that began with 10,000 grains and ended with 5000. The error bars here show the standard deviations magnified by a factor of 100.

Distributions

We also examine the distribution of grain topologies (number of sides) and areas for the different systems. Figures 3.27 and 3.28 show these distributions after the systems have evolved from 25,000 grains until only 5000 grains remain. Examination of the distribution of grain topologies in Figure 3.27 and of grain areas in Figure 3.28 shows that the Brakke and proposed methods yield nearly

identical results when refined. However, when unrefined, both methods yield results that diverge from their refined versions. In particular, the unrefined Brakke method produces more grains with small numbers of faces than both refined versions, whereas the unrefined proposed method produces fewer such grains. Likewise, in considering grain areas, the unrefined Brakke method produces too many very small grains, whereas the unrefined version of the proposed method produces too few, though the discrepancy here is much smaller.

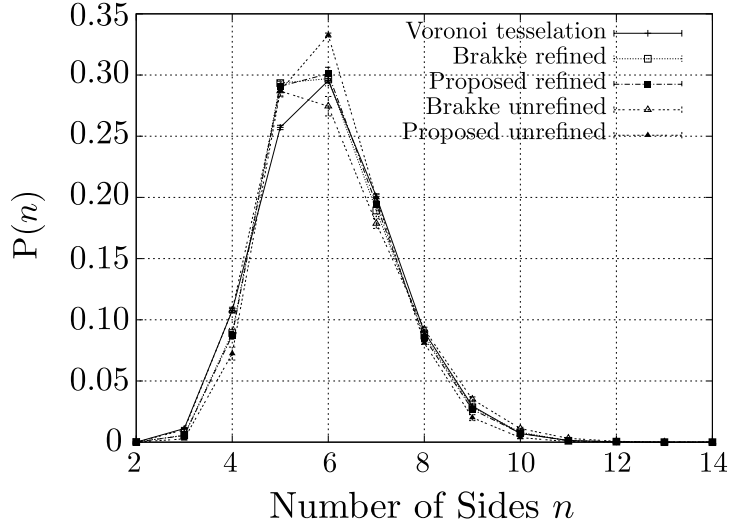


Figure 3.27: Topological (number of sides, n) distributions for microstructures evolved from four Voronoi tessellations of 25,000 grains until only a fifth of the grains remain.

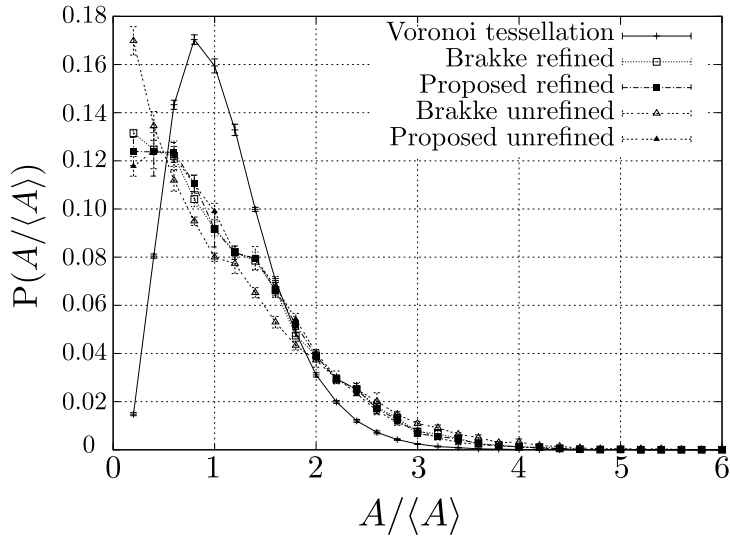


Figure 3.28: Normalized grain area distributions ($A/\langle A \rangle$) for microstructures evolved from four Voronoi tessellations of 25,000 grains until only a fifth of the grains remain.

The observation that simulations that produce too many grains of small areas also produce too

many grains of few sides and visa versa is not surprising in light of Lewis's Law [65, 66], which states that the area of a grain is linearly related to its number of sides. Moreover, the excess of small grains in the Brakke method on an unrefined mesh can be understood by reference to Figure 3.25. This figure shows that grains with few sides shrink more slowly than they should according to the von Neumann-Mullins exact result. We also note that this figure shows that large grains grow too slowly. This is also consistent with the distributions, although this effect is weaker.

3.7 Conclusions

The primary purpose of this chapter was to introduce curvature flow on two-dimensional cell structures and a method we use to simulate such systems. Although we report some data in this chapter, the bulk of our results are reported in Chapter 5, where we compare results from two- and three-dimensional systems.

In future work we might consider in greater detail simulations that begin from various initial conditions. J.K. Mason has done some work [67] in simulating systems that begin from a variety of initial conditions, including hexagonal cell structures into which some topological defects have been introduced (a system which exhibits very beautiful evolution). Considering various initial conditions will help us understand how curvature flow evolves cell structures towards a steady state that is independent of initial conditions.

We might also consider other dynamics on two-dimensional cell structures. One particular dynamic worth considering is the coarsening of foams. Although curvature flow also plays a role here, the evolution of these systems is qualitatively different from that considered in this chapter. This is due to the ability of gas to diffuse within a bubble rapidly and to allow the boundary to assume a minimal surface area with a fixed volume at a time-scale much faster than the diffusion of air through boundaries. J.K. Mason has performed some work on these systems, though the intrinsically non-local nature of this dynamic allows for the simulation of only relatively small systems [68].

One area that is also worthwhile pursuing is the case of anisotropic boundary energy and boundary mobility. That is, what happens when we consider systems in which the speed of a boundary's motion depends on the misorientation between two neighboring grains? How will this effect the steady state of our dynamical cell systems? This area has been studied extensively [69, 70, 71], though not with a precise front-tracking model like the one described here.

In a more theoretical vein, we would like to understand what types of events can occur in these

systems. We have pointed out that for curvature flow on closed, smooth curves, no singularities arise before the curve disappears as a circle. We can ask similar questions regarding continuous cell structures that evolve via curvature flow. For example, we have noticed in our simulations that edges never intersect except at triple points. In theory, can edges intersect at other places? In a similar vein we notice in our simulations that grains disappear with two or three sides. In theory, can grains with four or five sides disappear before becoming triangular? Once a system has reached steady state, at what frequencies do T1, T2, and T3 changes occur?